High-accuracy wavefront control for retinal imaging with Adaptive-Influence-Matrix Adaptive Optics

Weiyao Zou and Stephen A. Burns

School of Optometry, Indiana University, 800 East Atwater Avenue, Bloomington, Indiana 47405, USA
zouw@indiana.edu

Abstract: We present an iterative technique for improving adaptive optics (AO) wavefront correction for retinal imaging, called the Adaptive-Influence-Matrix (AIM) method. This method is based on the fact that the deflection-to-voltage relation of common deformable mirrors used in AO are nonlinear, and the fact that in general the wavefront errors of the eye can be considered to be composed of a static, non-zero wavefront error (such as the defocus and astigmatism), and a time-varying wavefront error. The aberrated wavefront is first corrected with a generic influence matrix, providing a mirror compensation figure for the static wavefront error. Then a new influence matrix that is more accurate for the specific static wavefront error is calibrated based on the mirror compensation figure. Experimental results show that with the AIM method the AO wavefront correction accuracy can be improved significantly in comparison to the generic AO correction. The AIM method is most useful in AO modalities where there are large static contributions to the wavefront aberrations.

References and links

1. H. W. Babcock, "Adaptive Optics Revisited," Science, **249**, 4966 pp. 253–257 (1990).
2. J. Liang, D. R. Williams, and D. T. Miller, "Supernormal vision and high-resolution retinal imaging through adaptive optics," J. Opt. Soc. Am. A **14**(11), 2884–2892 (1997).
3. N. Devaney, E. Dalimier, T. Farrell, D. Coburn, R. Mackey, D. Mackey, F. Laurent, E. Daly, and C. Dainty, "Correction of ocular and atmospheric wavefronts: a comparison of the performance of various deformable mirrors," Appl. Opt. **47**(35), 6550–6562 (2008).
4. A. Roorda, F. Romero-Borja, W. Donnelly Iii, H. Queener, T. J. Hebert, and M. C. W. Campbell, "Adaptive optics scanning laser ophthalmoscopy," Opt. Express **10**(9), 405–412 (2002), http://www.opticsinfobase.org/oe/abstract.cfm?URI=oe-10-9-405.
5. D. Huang, E. A. Swanson, C. P. Lin, J. S. Schuman, W. G. Stinson, W. Chang, M. R. Hee, T. Flotte, K. Gregory, C. A. Puliafito, and J. G. Fujimoto, "Optical coherence tomography," Science **254**(5035), 1178–1181 (1991).
6. J. G. Fujimoto, "Optical coherence tomography for ultrahigh resolution in vivo imaging," Nat. Biotechnol. **21**(11), 1361–1367 (2003).
7. D. T. Miller, J. Qu, R. S. Jonnal, and K. Thorn, "Coherence gating and adaptive optics in the eye," Proc. SPIE **4956**, 65–72 (2003).
8. B. Hermann, E. J. Fernández, A. Unterhuber, H. Sattmann, A. F. Fercher, W. Drexler, P. M. Prieto, and P. Artal, "Adaptive-optics ultrahigh-resolution optical coherence tomography," Opt. Lett. **29**(18), 2142–2144 (2004).
9. Y. Zhang, J. Rha, R. Jonnal, and D. Miller, "Adaptive optics parallel spectral domain optical coherence tomography for imaging the living retina," Opt. Express **13**(12), 4792–4811 (2005), http://www.opticsinfobase.org/oe/abstract.cfm?URI=oe-13-12-4792.
10. R. J. Zawadzki, S. M. Jones, S. S. Olivier, M. Zhao, B. A. Bower, J. A. Izatt, S. Choi, S. Laut, and J. S. Werner, "Adaptive-optics optical coherence tomography for high-resolution and high-speed 3D retinal in vivo imaging," Opt. Express **13**(21), 8532–8546 (2005), http://www.opticsinfobase.org/oe/abstract.cfm?URI=oe-13-21-8532.
11. E. J. Fernández, B. Povazay, B. Hermann, A. Unterhuber, H. Sattmann, P. M. Prieto, R. Leitgeb, P. Ahnelt, P. Artal, and W. Drexler, "Three-dimensional adaptive optics ultrahigh-resolution optical coherence tomography using a liquid crystal spatial light modulator," Vision Res. **45**(28), 3432–3444 (2005).
12. J. Rha, R. S. Jonnal, K. E. Thorn, J. Qu, Y. Zhang, and D. T. Miller, "Adaptive optics flood-illumination camera for high speed retinal imaging," Opt. Express **14**(10), 4552–4569 (2006), http://www.opticsinfobase.org/abstract.cfm?URI=oe-14-10-4552.

13. J. A. Martin, and A. Roorda, "Direct and noninvasive assessment of parafoveal capillary leukocyte velocity," Ophthalmology **112**(12), 2219–2224 (2005).
14. Z. Zhong, B. L. Petrig, X. Qi, and S. A. Burns, "In vivo measurement of erythrocyte velocity and retinal blood flow using adaptive optics scanning laser ophthalmoscopy," Opt. Express **16**(17), 12746–12756 (2008), http://www.opticsinfobase.org/abstract.cfm?URI=oe-16-17-12746.
15. H. Song, Y. Zhao, X. Qi, Y. T. Chui, and S. A. Burns, "Stokes vector analysis of adaptive optics images of the retina," Opt. Lett. **33**(2), 137–139 (2008).
16. N. Doble, G. Yoon, L. Chen, P. Bierden, B. Singer, S. Olivier, and D. R. Williams, "Use of a microelectromechanical mirror for adaptive optics in the human eye," Opt. Lett. **27**(17), 1537–1539 (2002).
17. D. X. Hammer, R. D. Ferguson, C. E. Bigelow, N. V. Iftimia, T. E. Ustun, and S. A. Burns, "Adaptive optics scanning laser ophthalmoscope for stabilized retinal imaging," Opt. Express **14**(8), 3354–3367 (2006), http://www.opticsinfobase.org/oe/abstract.cfm?URI=oe-14-8-3354.
18. D. C. Gray, W. Merigan, J. I. Wolfing, B. P. Gee, J. Porter, A. Dubra, T. H. Twietmeyer, K. Ahamd, R. Tumbar, F. Reinholz, and D. R. Williams, "In vivo fluorescence imaging of primate retinal ganglion cells and retinal pigment epithelial cells," Opt. Express **14**(16), 7144–7158 (2006), http://www.opticsinfobase.org/oe/abstract.cfm?URI=oe-14-16-7144.
19. D. Merino, C. Dainty, A. Bradu, and A. G. Podoleanu, "Adaptive optics enhanced simultaneous en-face optical coherence tomography and scanning laser ophthalmoscopy," Opt. Express **14**(8), 3345–3353 (2006), http://www.opticsinfobase.org/oe/abstract.cfm?URI=oe-14-8-3345.
20. Y. Zhang, S. Poonja, and A. Roorda, "MEMS-based adaptive optics scanning laser ophthalmoscopy," Opt. Lett. **31**(9), 1268–1270 (2006).
21. S. A. Burns, R. Tumbar, A. E. Elsner, D. Ferguson, and D. X. Hammer, "Large-field-of-view, modular, stabilized, adaptive-optics-based scanning laser ophthalmoscope," J. Opt. Soc. Am. A **24**(5), 1313–1326 (2007).
22. M. Born, and E. Wolf, Principles of Optics, 7th Ed., (Cambridge University Press, Cambridge, 2001) p.528.
23. D. C. Chen, S. M. Jones, D. A. Silva, and S. S. Olivier, "High-resolution adaptive optics scanning laser ophthalmoscope with dual deformable mirrors," J. Opt. Soc. Am. A **24**(5), 1305–1312 (2007).
24. R. J. Zawadzki, S. S. Choi, S. M. Jones, S. S. Oliver, and J. S. Werner, "Adaptive optics-optical coherence tomography: optimizing visualization of microscopic retinal structures in three dimensions," J. Opt. Soc. Am. A **24**(5), 1373–1383 (2007).
25. W. Zou, X. Qi, and S. A. Burns, "Wavefront-aberration sorting and correction for a dual-deformable-mirror adaptive-optics system," Opt. Lett. **33**(22), 2602–2604 (2008).
26. http://www.imagine-eyes.com/content/view/45/103/.
27. Specifications of product Model No. μDM140–450-E-AgMgF, SN: 09w200#108–450D16–9, Boston MicroMachines Corporation (2007).
28. J. B. Stewart, A. Diouf, Y. Zhou, and T. G. Bifano, "Open-loop control of a MEMS deformable mirror for large-amplitude wavefront control," J. Opt. Soc. Am. A **24**(12), 3827–3833 (2007).
29. S. Thomas, T. Fusco, A. Tokovinin, M. Nicolle, V. Michau, and G. Rousset, "Comparison of centroid computation algorithms in a Shack-Hartmann sensor," Mon. Not. Astron.Soc. **371**(1), 323–336 (2006).
30. E. J. Fernandez, L. Vabre, B. Hermann, A. Unterhuber, B. Povazay, and W. Drexler, "Adaptive optics with a magnetic deformable mirror: applications in the human eye," Opt. Express **14**(20), 8900–8917 (2006), http://www.opticsinfobase.org/oe/abstract.cfm?URI=oe-14-20-8900.
31. Y. Zhou, "A confocal microscope using adaptive optics," Master thesis, Boston University, 2005.
32. Y. Zhou, and T. Bifano, "Characterization of Contour Shapes Achievable with a MEMS Deformable Mirror," Proc. SPIE **6113**, 123–130 (2006).
33. J. W. Evans, B. Macintosh, L. Poyneer, K. Morzinski, S. Severson, D. Dillon, D. Gavel, and L. Reza, "Demonstrating sub-nm closed loop MEMS flattening," Opt. Express **14**(12), 5558–5570 (2006), http://www.opticsinfobase.org/oe/abstract.cfm?URI=oe-14-12-5558.
34. W. Zou, and S. A. Burns, "Improve adaptive optics wavefront control accuracy for retinal imaging with dual-influence-matrix method," in 2009 ARVO Annual meeting, Poster D960, Program NO. 1052, Fort Lauderdale, Florida, May 3–7 (2009).
35. V. N. Mahajan, "Strehl ratio for primary aberrations in terms of their aberration variance," J. Opt. Soc. Am. **73**(6), 860–861 (1983).
36. H. Hofer, P. Artal, B. Singer, J. L. Aragon, and D. R. Williams, "Dynamics of the eye's wave aberration," J. Opt. Soc. Am. A **18**(3), 497–506 (2001).
37. N. Davies, L. Diaz-Santana, and D. Lara-Saucedo, "Repeatability of ocular wavefront measurement," Optom. Vis. Sci. **80**(2), 142–150 (2003).
38. T. Salmon, and L. Thibos, "Videokeratoscope-line-of-sight misalignment and its effect on measurements of corneal and internal ocular aberrations," J. Opt. Soc. Am. A **19**(4), 657–669 (2002).

1. Introduction

The human retina is a thin and delicate tissue that supports a number of types of cells organized in discrete layers. The ability to resolve single cells noninvasively in the living retina is of growing importance in the study of retinal diseases and can potentially provide important data for evaluating the efficacy of new therapies. However, high resolution imaging of the retina through the natural pupil of the eye is extremely difficult due to the optical

aberrations in the cornea and crystalline lens and the eye's tear film. Adaptive optics (AO), a technique that originated in astronomy for correcting air turbulence [1], can remove the imaging blur and sharpen the images of the retinal cellular structures *in vivo* [2]. A Shack-Hartmann wavefront sensor is usually used to measure the wavefront error, and a deformable mirror (DM) is employed to correct the wavefront error to improve the imaging resolution [3]. In vision science and biomedical imaging, AO can increase both lateral and axial resolution in confocal fundus imaging [2,4]. The Adaptive Optics Scanning Laser Ophthalmoscope (AOSLO) [4], a confocal Scanning Laser Ophthalmoscope (SLO) equipped with adaptive optics, allows the improved *en face* imaging of retinal tissue *in vivo*. When integrated with optical coherence tomography (OCT) [5,6], AO can significantly improve the lateral resolution of OCT imaging, yielding three-dimensional high-resolution volumetric image [7–11]. AO is also applicable in other imaging and measurement modalities including flood-illuminated imaging [12], retinal blood flow measurement [13,14], and polarization-sensitive imaging [15].

Many AO systems for human retinal imaging with SLO or OCT have been successfully built [2,4,8–10,16–21]. As a metric to evaluate the AO performance, the root-mean-square (RMS) values of the residual wavefront error of the above mentioned systems were reported to be around 0.07 to 0.2 micron (µm) over a pupil of 6-7 mm or smaller, yielding the Strehl ratios of their imaging systems ranging from 0.2 to 0.76. Many AO systems work in the near infrared. Given the commonly used light source for retinal imaging, a Super Luminescent Diode (SLD) with the central wavelength λ of 840 nanometer (nm), the Marechal Criterion for Rayleigh diffraction limit can be generally expressed as an RMS wavefront of about 0.06 µm (λ/14) [22]. To yield "good" diffraction-limited imaging with a Strehl ratio of 0.92, the RMS wavefront should be controlled to less than 0.04 µm (λ/21). Compared with these criteria, the existing AO correction systems do not produce diffraction-limited retinal imaging in general. Therefore, it is still useful to improve AO systems.

To increase the dynamic range and improve the precision of wavefront correction, the Woofer-Tweeter dual DM approach was introduced [23,24], and a novel wavefront control algorithm was proposed to simultaneously optimize both DMs with the damped least-squares method [25]. The Woofer-Tweeter dual DM approach can efficiently improve wavefront correction efficiency using either sequential or simultaneous wavefront control optimization approach [23–25]. However, even ignoring the dynamic variations in the wavefront error during *in vivo* imaging, the wavefront correction precision is still limited by many factors, such as the precision of the wavefront sensor (typically a Shack-Hartmann wavefront sensor), the precision of positioning the DM actuators, and the accuracy of the influence matrix measurement as well as the noise level of the measurements. In this paper, we propose an approach to improve the accuracy of influence matrix measurement by better accounting for the nonlinearity effect of the so-called deflection-to-voltage relation of the DMs.

The Woofer-Tweeter AO system used for these measurements is shown in Fig. 1. The light source is generated by an SLD with the central wavelength of 676 nm, and it is collimated by a collimation lens to illuminate the aberration sample. The aberration sample is optically conjugated to the Woofer DM, which is in turn conjugated to the Tweeter DM, and is finally imaged onto the lenslet array of the Shack-Hartmann wavefront sensor by a series of relay lenses. A second CCD camera is used to display the point spread function (PSF) of the AO system, and a light-emitting-diode (LED) is used to generate a reference light source for the Shack-Hartmann sensor. In this system, the Woofer is an electromagnetic mirror called the Mirao-52d DM, a product of Imagine Eyes [26], while the Tweeter is a 140-actuator MEMS mirror manufactured by the Boston Micromachines Corporation (BMC) [27].
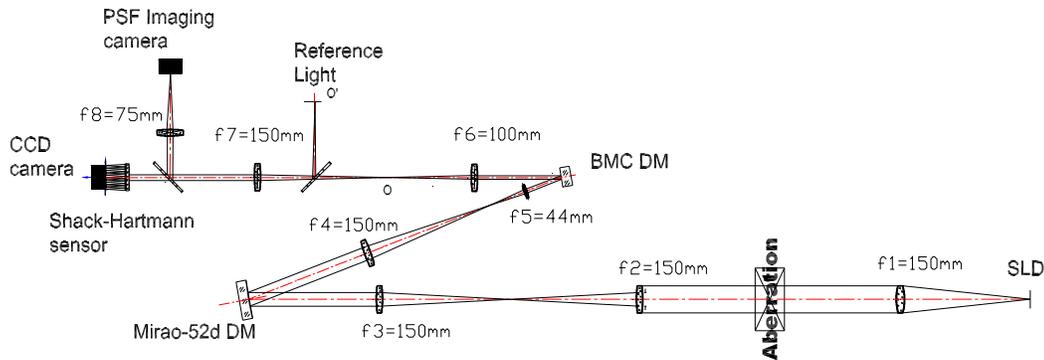
Fig. 1. Optical layout of the Woofer-Tweeter adaptive optics Testbed system

2. Methods

2.1 DM characterization

For a continuous DM, applying a voltage to an actuator to push or pull the mirror results in a mirror deflection (or mirror surface displacement). The relation between the DM mirror deflection and the actuator voltage applied is called the deflection-to-voltage (D-V) relation. The D-V relation behavior is usually nonlinear, and the mirror displacement at a given actuator is spatially coupled with the adjacent actuators [28]. Generally the influence function of an actuator is defined as the mirror deflection change at a given unit actuator voltage value, while in this paper the influence matrix of an AO system is defined as the matrix of wavefront slope changes at a unit value of actuator voltage applied.

In this study, the D-V relation of an actuator was calibrated as follows: First, the DM actuator voltages were set to place all actuators at the middle position of the actuator dynamic range. The wavefront for this position was measured by the Shack-Hartmann sensor and used as the reference wavefront. Second, the mirror was pushed (or pulled) by the actuator with a series of voltages that spanned its full dynamic range, which was from −0.95 volts to 0.95 volts with an increment of 0.2 volts for the Mirao-52d DM, and from 0 to 230 volts with an increment of 20 volts for the BMC DM. At each increment, the changed wavefront was measured by the Shack-Hartmann sensor. The peak-to-valley (p-v) value of the wavefront difference map between the changed wavefront and the reference wavefront is actually twice that of the mirror deflection at the given pushing (or pulling) actuator. Therefore, the D-V relation of each actuator can be calibrated in sequence.

For our experimental system, the field of view for each lenslet was 35 × 35 pixels on the CCD camera, and each Shack-Hartmann spot was approximately 5 × 5 pixels (The theoretical Airy disc size is 5.2 × 5.2 pixels). The focal length of the lenslets was 7.6 mm, and the pitch size of the lenslets was 0.3×0.3 mm^2. The centroid of the Shack-Hartmann spot was estimated by evaluating the center of gravity of the spot irradiance within each subaperture. As shown in the previous literature [29], the centroid measurement is linear for this configuration as long as the entire spot remains within the subaperture.

2.1.1 D-V relation of the Mirao-52d DM

Figure 2 presents the D-V relations of the Mirao-52d DM. Note that the D-V relation of each actuator is almost linear [30], but from the DM boundary to the DM center the nonlinearity increases. This phenomenon can be explained by the limitation of clear aperture of the DM. The size of the Mirao-52d DM mirror is 20 mm in diameter, but its clear aperture is only 15 mm. Because the boundary is constrained, an influence function can have its maximum deflection peak only for the actuators within the clear aperture. In addition, actuators outside the clear apertures are only measured on the flanks of their influence functions. This is shown

in Fig. 3 where the influence function of a boundary actuator (No. 44, using the Mirao specifications in this paper) is blocked in part by the aperture rim, while the influence function of a central actuator (No. 22) is circularly apodized. The highest degree of nonlinearity is found at actuator No. 22, whose D-V relation can be fitted (in μm) as

$$f_1(v) = 2.5457v^4 - 5.7316v^3 - 2.9065v^2 + 25.572v + 0.0697, \quad (R^2 = 1) \qquad (1)$$

where v is in volt. As shown in Fig. 2, for the actuators located outside the clear aperture of the DM, the nonlinearities of their D-V relations are mitigated because the Shack-Hartmann wavefront sensor may miss the maximum peaks of their mirror deflections.
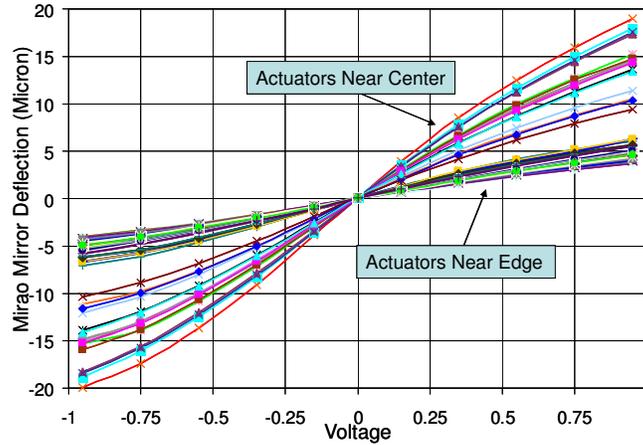
Fig. 2. D-V relations of the actuators of the Mirao DM. The response was systematic, with the central actuators having the largest deflections, and the highest degree of nonlinearity.
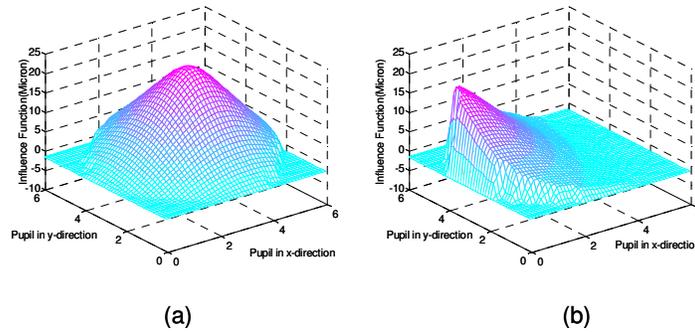
Fig. 3. Influence functions of (a) a central actuator (No. 22) and (b) an edge actuator (No. 44) of the Mirao DM. For these measurements all other actuators were held at zero volts.

On the other hand, the mirror influence function is also affected by both the mirror local deflection, and further the global figure of the mirror. To confirm this we changed the base figure shape of the mirror from approximately a flat profile, with all other actuators set at zero volts, to a series of varying levels of defocus. The actuator voltages for generating a given defocus were calculated with the least-squares method according to the initial influence matrix. The influence function of each actuator was calibrated in the presence of a given defocused mirror figure. In this paper the height of an influence function is defined as the p-v value of the mirror deflection change at a unit value of actuator voltage, which is only one-half of the p-v value of the corresponding wavefront difference. Experimental calibration showed that the relation between the influence function height and the given wavefront

defocus is approximately linear, but with different slopes. Figure 4 plots such slopes for each actuator of the Mirao DM, showing that the rate of the influence function change with defocus in diopter (D) depends on the location of the actuator: Larger slopes (>5µm/D) for the actuators inside the aperture, and smaller slopes (<4µm/D) for actuators outside of the aperture. The slopes of boundary actuators are about 4-5 µm/D.
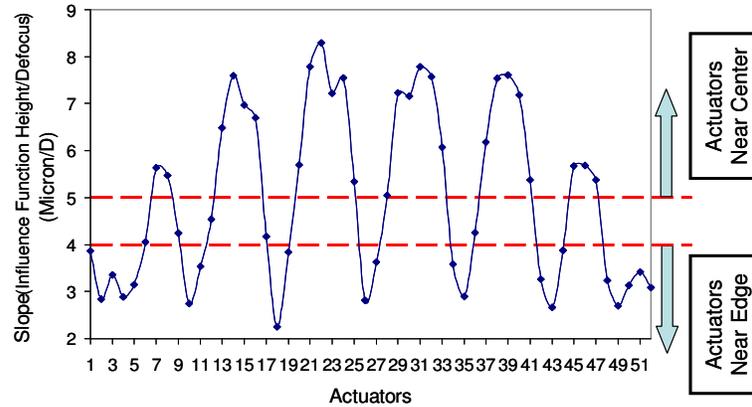
Fig. 4. Plot of slopes of the influence function as a function of wavefront defocus for the Mirao DM
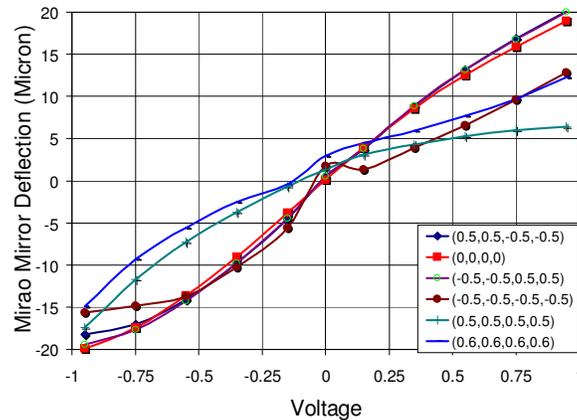
Fig. 5. D-V relations of the Mirao-DM central actuator (No. 22) at the variations of its neighboring actuators. Each curve represents the D-V relation of that actuator at different set of voltages applied to its four neighboring actuators.

The D-V relation of an actuator is also very sensitive to its local mirror figure. Figure 5 demonstrates this complexity. Curve (0, 0, 0, 0) is the D-V relation of a central actuator (No. 22) described by Eq. (1), where the four parameters (0, 0, 0, 0) represent the voltages of its four neighboring actuators. As shown in Fig. 5, the shape of the D-V curve varies remarkably when we push or pull its diagonal neighbors to construct a local astigmatism or local defocus mirror figure. Because the coupling of mirror figure to the actuator influence function is nonlinear, in general the D-V relation is complex. Any actuator stroke height variation in the neighborhood will induce a change in the D-V relation of that actuator, and the behavior of the D-V relation is hard to predict.
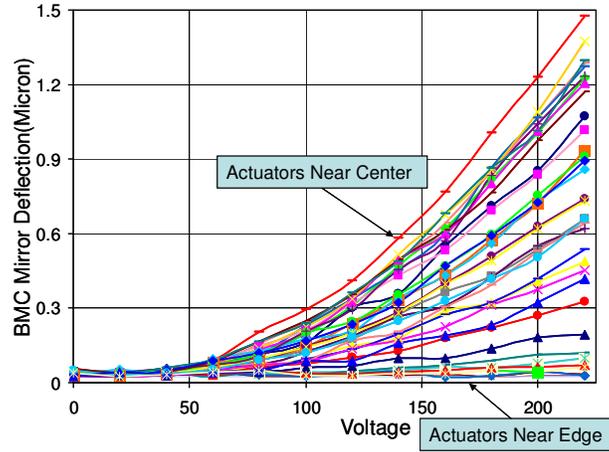
Fig. 6. D-V relations of the actuators located in the 1st quarter of the BMC DM.

2.1.2 D-V relation of the BMC DM

The MEMS DM is operated at a bias voltage, and we use a 150-volt bias voltage to approximately produce a mid-deflection. The nonlinearity of the D-V relation of the MEMS DM has been studied by many authors [31–33]. Physically, the nonlinearity is due to the increasing imbalance between the electrostatic force of activating an actuator and the mechanical restoring force with an increase of applied voltage [28]. To measure the nonlinearity of the BMC DM, the D-V relation of each actuator was calibrated from 0 to 230 volts with an increment of 20 volts, and the results are plotted in Fig. 6. The highest D-V nonlinearity was found at a central actuator, whose curve can be formulated (in µm) as

$$f_2(v) = -2.0 \times 10^{-8} v^3 + 4.15 \times 10^{-5} v^2 - 1.42 \times 10^{-3} v + 0.039, \quad (R^2 = 0.9995) \quad (2)$$

where v is in volt.

In this section, we have shown that the D-V relations of both Mirao DM and BMC DM are nonlinear. As a comparison, the D-V relation of the Mirao DM is less nonlinear, but it is related to both overall mirror figure and local mirror deflections. Thus, although the Mirao DM has a larger dynamic range for high-amplitude wavefront aberration correction, the generic influence matrix, which is usually calibrated at the flat mirror profile where the actuator stroke values are usually "zero", becomes inaccurate for high-amplitude wavefront error corrections.

2.2 Adaptive-Influence-Matrix AO correction

Due to the nonlinearity of the D-V relation of each actuator, to produce an accurate mirror deflection figure for compensating a given wavefront error requires an influence matrix that is accurate for the mirror at that deflection figure. An error in the influence matrix will produce an unintended change in mirror deflection. Even in the absence of noise this error could cause the wavefront correction to oscillate during convergence. Therefore, the accuracy of wavefront control to a large extent depends on how accurate we can calibrate the actuator influence functions and thereby the DM influence matrix for a specific AO system. As discussed in the previous section, the generic influence matrix is accurate for low-amplitude wavefront corrections, but not for high-amplitude wavefront correction. To solve this problem, we propose a new approach for influence matrix calibration, called the Dual Influence Matrix (DIM) method [34].
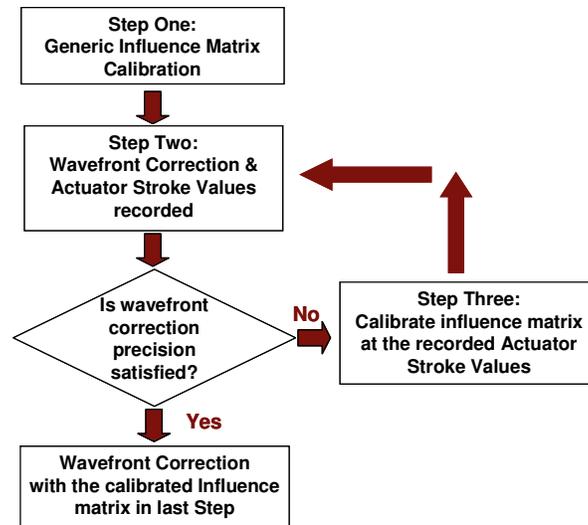
Fig. 7. Flow chart of influence matrix calibration with the AIM method

The influence matrix for correcting an high-amplitude wavefront aberration can be calibrated at the mirror deflection profile demanded for compensating that aberration; therefore, the obtained mirror influence functions will be accurate for the set of actuator strokes that defines the mirror deflection figure.

To implement the DIM method, the following procedures can be used: Step One, a generic influence matrix is calibrated at the mid-position of the DM dynamic range, where the mirror is usually approximately flat. Step Two, an AO wavefront correction is performed with the generic influence matrix until it converges, and then the accumulated actuator voltage values applied to the DM are recorded. Step Three, the DM influence matrix is recalibrated at the mirror deflection profile generated by the actuator stroke values recorded in Step Two.

To further improve the accuracy of influence matrix calibration, the DIM method can be employed iteratively as shown in Fig. 7, and then we have the Adaptive Influence Matrix (AIM) method, because in this method the influence matrix is calibrated adaptively to accommodate the more and more accurate mirror compensation figure demanded for the high-accuracy wavefront correction. If the wavefront correction accuracy is satisfied at Step Two, the influence matrix calibration process will be terminated, and the AO wavefront correction will continue with the new influence matrix calibrated. Otherwise, the loop will go to Step Three, and the iteration continues until it satisfies a set criteria. Obviously, the AIM iterative method becomes the DIM method when it has only one loop of iteration.

3. Experimental results

3.1 Validation of the DIM method

We implemented the proposed DIM and AIM methods in the system described in Fig. 1. The Lagrange multiplier-based damped least-squares algorithm was adopted for the wavefront correction control [25]. This wavefront correction algorithm sorts the wavefront aberrations into two groups: One group is the high-amplitude, low-order aberrations for the Mirao-52d DM, and another one is the low-amplitude, high-order aberrations for the BMC DM. According to the damped least-squares estimation, the actuator stroke vectors $\mathbf{X}$ ($|x_i|$<1.0 volts, i = 1, 2, …, 52) for the Mirao-52d DM and $\mathbf{Y}$ ($0< y_i$ <230 volts, i = 1, 2, …, 140) for the BMC DM can be computed by [25]

$$\begin{bmatrix} \mathbf{X} \\ \mathbf{Y} \end{bmatrix} = \begin{bmatrix} \mathbf{A}^T\mathbf{A} + \lambda_1 & \beta\mathbf{A}^T\mathbf{B} \\ \beta\mathbf{B}^T\mathbf{A} & \beta^2\mathbf{B}^T\mathbf{B} + \lambda_2 \end{bmatrix}^{-1} \begin{bmatrix} \mathbf{A}^T \\ \beta\mathbf{B}^T \end{bmatrix} \mathbf{S}, \tag{3}$$

where $\mathbf{A}$ is the influence matrix of the Mirao-52d DM, and $\mathbf{B}$ is the influence matrix of the BMC DM. In our experiment, the Lagrange multiplier was $\beta = 1.0$, the control gain was 0.6, the damping factor was $\lambda_1 = 20$ for the Mirao DM, and $\lambda_2 = 0.06$ (or 0.08) for the BMC DM.
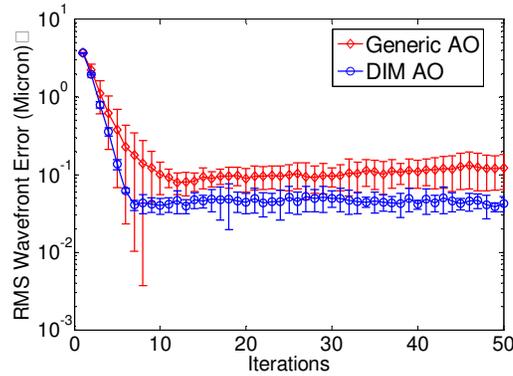
Fig. 8. Comparison of wavefront error reductions of the Generic AO and the DIM AO

The initial wavefront aberration was 3.72 µm in RMS, most of which was the low-order aberrations generated by a combination of two trial lenses (−0.5D astigmatism + 0.5D spherical) over a 15-mm pupil, and the rest were the systematic errors from the experimental system and the non-ideal performance of the trial lenses. We first implemented a generic influence matrix as described above and ran the AO control algorithm. Once the control converged, we recalibrated the influence matrix at the new resting point with the DIM method and restarted the control loop. Figure 8 compares the RMS wavefront error reductions between the generic AO method and the DIM AO method. Each curve was obtained by averaging six sets of experimental data for each method with the error bars indicating standard deviations. According to these curves, the residual RMS wavefront error of the generic AO method was reduced to about 0.11 µm with a standard deviation of about 0.02µm, while the residual RMS wavefront error of the DIM AO method was about 0.046 µm with a standard deviation of about 0.003µm. Given the wavelength of the SLD light source at 676.6 nm used in our system, a 0.046-µm RMS wavefront error means an imaging Strehl ratio of 0.83 according to Mahajan's approximation [35]. Both the rate of convergence and the final Strehl ratios were improved.

3.2 Test of the AIM method

To test the extent to which we could improve wavefront control using the AIM method we performed an additional experiment. The Woofer-Tweeter AO system was further optimized, because for high-accuracy wavefront control, a careful choice of control parameters is as critical as the accurate calibration of the influence matrix. We first decreased the gain of the feedback loop to 0.5, while the damping factor was set to $\lambda_1 = 10$ for the Mirao-52d DM and to $\lambda_2 = 0.05$ for the BMC DM. Because we need the BMC DM to operate near its midpoint, we then re-calibrated the influence functions using a smaller value of differential voltage to make sure the calibration is accurate.

The testing sample used for generating wavefront aberrations was a combination of two trial lenses (−0.5D astigmatism + 0.12D spherical) over a 15-mm pupil, yielding the initial RMS wavefront error of 3.4µm. Since our Mirao DM had problems with heating, a little compromise in amplitude of wavefront aberration should make the performance of the Mirao DM more reliable, because the AIM method takes more iterations than the DIM method does.

Figure 9(a) shows the evolution of the RMS error during the wavefront control for several corrections cycles using the AIM method.
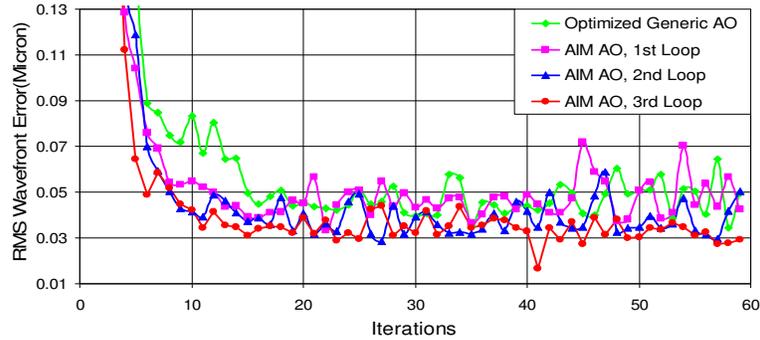
(a)
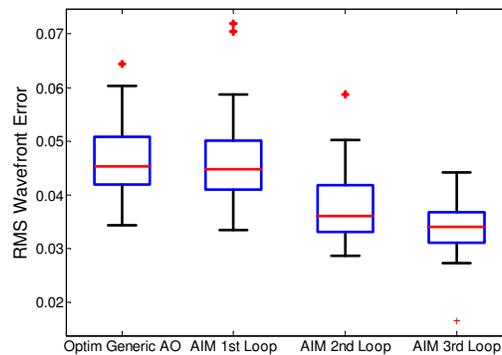
(b)

Fig. 9. (a) Wavefront error reduction during AO control loops for the AIM method. Most of the improved convergence rate occurs after the first step in wavefront error reduction. (b) Bartlett multiple-sample test for equal variances: Box and whisker plots for the final 45 iterations of each AIM Loop in sequence.

The average RMS error and Strehl ratio (SR) for the final 45 points of the Generic, AIM 1st loop, AIM 2nd loop and AIM 3rd loop curves were 0.0466 µm (SR 0.82), 0.0470 µm (SR 0.83), to 0.0383 µm (SR 0.88), and 0.0338 µm (SR 0.91) respectively. AIM succeeded in decreasing the RMS error gradually in successive loops (ANOVA, $p < 0.05$), and the iterative process is converging. The RMS variance for the final AIM loop (0.005 µm) was slightly decreased (Bartlett multiple-sample test for equal variance, $p < 0.05$), but not for the other loops (0.007~0.008 µm). Thus the wavefront control of the AIM AO method is stable, and the control accuracy can be even higher. The standard deviation of the residual wavefront RMS (after 15 iterations) is decreased, and the speed of convergence is increased.

4. Discussion and Conclusions

Most existing AO control techniques are most efficient for low-amplitude and low-order wavefront error corrections in both biomedical and astronomical applications. In retinal imaging a generic AO can typically reduce the RMS wavefront error to around 0.1 µm or a bit better. To further improve the AO correction becomes challenging in practice due to errors in control matrix and control parameters, the errors due to noise and actual oscillations in the eyes aberrations [36,37]. In this paper we show that, by accounting for the presence of static aberration, the AIM method increases the accuracy of wavefront correction and decreases the noise in AO control. With a Woofer-Tweeter testbed system, the AIM method can further

reduce the residual RMS wavefront error of a generic AO, from 0.01 µm to about 0.035 µm, corresponding to an increase in the Strehl ratio from 0.50 to 0.90 at the wavelength of 676.6 nm.

In ophthalmic AO, the largest ocular aberrations are quasi-static and low-order errors (essentially defocus and astigmatism) [36–38]. That is, the average DM deflection required for imaging a subject with 4D of spherical error (defocus) is very large relative to the dynamic changes of AO correction around this operating point. Therefore, given an AO system and a subject, the AIM AO approach can be performed at the beginning of the imaging session, and the accurate influence matrix obtained is good for the rest of the experimental session. In practice repeatedly recalibrating the influence matrix in a dynamic AO imaging session is not required.

In principle a complete solution for AO correction with large-amplitude wavefront errors is to fully model the DMs, yielding a pre-calibrated Look-Up Matrix Table (LUMT). This would in principle allow AO correction with different wavefront aberrations without any additional measurements. However, there is a straightforward, practical approximation, which would involve pre-measurement of a series of influence matrices, corresponding to different defocus levels encountered in the human population (say at 1D step). When a subject is first run, the system can use the generic influence matrix to find the appropriate defocus, and then the closest appropriate influence matrix will be loaded from the LUMT and used "on the fly". The LUMT approach for ophthalmic AO is very simple and does not require increased subject time because all the influence functions are pre-calibrated.

As an alternative approach to LUMT, the AIM method is much simpler than determining the full model of the mirrors in practice. It is important to note that the AIM AO method can be generalized to any AO modality where there is a significant static contribution to the wavefront error.

Acknowledgements